PRESSURE PIV ANALYSIS OF A HOVERING UAS ROTOR WAKE

Adam Nickels
Fluids Research Department
The Pennsylvania State University
PO Box 30, State College, PA 16804
asn99@psu.edu

James Goldschmidt
Fluids Research Department
The Pennsylvania State University
PO Box 30, State College, PA 16804
jzg6181@psu.edu

Matthew Bross
Fluids Research Department
The Pennsylvania State University
PO Box 30, State College, PA 16804
mqb6401@psu.edu

Jeff Harris
Fluids Research Department
The Pennsylvania State University
PO Box 30, State College, PA 16804
jeff.harris@psu.edu

ABSTRACT

The abundance and complexity of Unmanned Aerial Systems (UAS), specfially quad-copters, has resulted in the need for the study and development of more accurate noise prediction models, onboard sensor packaging, and noise-based design constraints. While much can be learned through acoustic array and velocity field measurements, information gained from knowledge of the full pressure field can aid in these goals. This work presents a variational Bayesian inverse reconstruction framework for conservative pressure-gradient dynamics, computed using high-speed particle image velocimetry and measured pressure microphone data, applied to the flow field of a hovering UAS rotor. This framework allows for physically meaningful residual interpretation together with explicit and spatially adaptive uncertainty modeling.

INTRODUCTION

Unmanned Aerial Systems (UAS) specifically small quad-copters are becoming more abundant in both commercial and research applications. The noise from this new class of air vehicles can be looked at as a superposition of the tonal, broadband, and impulsive noise sources from the rotors and air-frame, and the complexity of these vehicles makes it imperative to determine the relative importance of each noise source for guiding design strategies (Rizzi *et al.* (2020)). While rotor noise has received significant attention in recent years, airframe noise and the wake pressure field responsible for it has received much less focus. The need for investigating this noise source is amplified by the fact that most quadcopter configurations have airframes in near proximity to the rotor. This leads to the highly turbulent wake pressure impinging on it, which as explained by Curle (1955) acoustic analogy will propagates as noise. Two recent notable airframe interaction noise investigations for booms below lifting UAS rotors in forward flight (Zhu *et al.* (2021)) and in hover (Zawodny & Boyd (2020)) found that the boom acts as a partial ground plane causing an unsteady increase in unsteady pressure around the rotor blade relating to increased tonal noise levels. More complex installations were investigated numerically by Jia & Lee (2019, 2020) and experimentally by Zawodny & Pettingill (2018) for quadcopter configurations in forward flight. Both studies showed that unsteady pressure fluctuations on the airframe caused by interactions with the convecting rotor wake increased broadband and tonal noise levels. These studies establish the importance of rotor airframe interaction noise, but pay little attention to the unsteady wake pressure field generating it.

For airframe interaction noise modeling it is important to not only model the point-wise wake pressure spectrum, but also the spatial pressure coherence related to the noise source strength. Two recent examples of design strategies which rely on de-correlating pressure fluctuations on the airframe to reduce noise are the use of permeability by Cantos *et al.* (2024) and the addition of rotor boom curvature by Wiedemann *et al.* (2025). Another area that also deserves attention in the matter of spatial wake pressure variations is the implementation of pressure and acceleration sensors below UAS vehicles. These systems need to be protected from large pressure fluctuations and therefore a spatially resolved models of the unsteady wake pressure are needed for both intelligent sensor placement and sensor denoising. Further design improvements could undoubtedly be achieved with improved measurements of the wake pressure field, but this is very difficult to achieve due to the cost prohibitive nature of implementing many pressure sensors which also inherently alter the measured field. That is why we are investigating the feasibility of performing non-intrusive pressure field estimations from high-speed stereo particle image velocimetry (PIV) measurements. Although wake PIV measurements are not new, the goal is that through applying this newly developed variational Bayesian inverse reconstruction framework the resulting pressure fields can be used in the future to inform both wake pressure models and vehicle / sensor placement design strategies.

In this study we investigate the unsteady pressure field in the wake of a hovering UAS rotor through a combination of high-speed PIV and pressure PIV. This analysis incorporates pressure microphones in the wake and a spatially adaptive inverse algorithm to reconstruct pressure and spatial confidence using PIV-derived forcing. This methodology constitutes a variational Bayesian inverse reconstruction framework for conservative pressure-gradient dynamics, allowing physically meaningful residual interpretation together with explicit and spatially adaptive uncertainty modeling (van Oudheusden, 2013*a*; Zhang *et al.*, 2020*a*; Azijli *et al.*, 2016). The wake pressure field will be analyzed to determine the feasibility of obtaining the spatially resolved pressure field from planar measurements. In what follows, we will start by describing the experimental facility and test condition. This is then followed by a description of the pressure PIV application. Then a current result will be shown and followed by a description of additions for a future paper.

FACILITY AND EXPERIMENTS

The experiments were conducted in The Pennsylvania State Applied Research Laboratory (Penn State ARL) flow through anechoic chamber (Goldschmidt *et al.*, 2026). The anechoic facility is 9.3 m high by 5.5 m wide by 6.9 m deep. The fiberglass wedges are approximately 0.9 m and the facility has been found to be anechoic down to 90 Hz based on ISO 3745 specifications. The facility additionally contains a fan for recirculating flow-through conditions, but this was not utilized in this experimental campaign.

An APC 12x6E rotor Advanced Precision Composites (2026) with a 0.1524 m radius (R) was used for the hovering rotor experiments. The rotor was mounted to a test stand shown in Figure 1 which included a KDE 3510XF-475 motor, a KDE-UAS-55HVC ESC for motor speed control, and a Futek MBA500 two-axis load cell for measuring mean thrust and torque coefficients. The load cell was sampled at 10 kHz. Attached to the test stand were three PCB 377C10 1/4" pressure microphones for measuring the unsteady pressure in the rotor wake. The wake microphones were located at radial distances of 0.5R, 0.66R and 0.95R from the rotor center and 0.5R below the rotor tip path and act as boundary conditions for the pressure reconstruction. Additionally three 1/2" PCB 377B02 free-field microphones were placed in the far-field of the rotor at a radial distance of 16R and with polar angles of 0° in the rotor plane, and -10° and -20° below the rotor plane. The microphones were sampled at 51.2 kHz. The nominal rotor speed was 5400 RPM giving a tip Mach number of 0.25 and all data was collected for 90s. The measured time averaged thrust coefficient C_t was 9.9x10^{-3} and torque coefficient C_q was 2.4x10^{-3}.

High-speed stereoscopic particle image velocity (PIV) measurements were made in a plane perpendicular to the rotor rotation direction to measure the out of plane (u_z), radial (u_x), and vertical (u_y) velocity components of the wake flow field as shown in Figure Figure 1. The flow was seeded with atomized DEHS tracer particles and the flow was illuminated with a 3 mm thick laser sheet generated by a Photonics DM50 High-speed laser operating in single-pulse mode. The particle images were captured with two Phantom VEO 1310 cameras fitted with 100 mm Zeiss lenses, 2x teleconverters, and Scheimpflug adapters to account for the out of plane camera alignment. Images were acquired at a rate of 9 kHz or approximately 100 frames per rotor revolution for a total of 40260 images. Image pre- and post-processing were performed in the Davis 10.2 software. Errors in the individual vectors were estimated to be approximately 3% of the mean velocity as determined by the routines in the DaVis software.

PRESSURE FROM PIV

Pressure is typically estimated by integrating the momentum equation, which provides a direct relationship between a given velocity field and a desired pressure field. As shown in Equation 1, the gradient of the pressure field is a function of the material derivative and velocity vector data obtained by simulation, Particle Image Velocimetry (PIV), or Particle Tracking Velocimetry (PTV) measurements can used to compute the input source ($f(u)$). In certain cases the material derivative of velocity can be calculated directly by taking the time derivative of particle velocities or the second time derivative of particle locations (Liu & Katz, 2006). However, for typical velocity vector data, Equation 2 is solved for the material derivative, in an Eulerian framework. Once the source term is calculated, the field can be integrated for pressure, provided an initial boundary condition is specified (Charonko *et al.*, 2010; van Oudheusden, 2013*b*; Zhang *et al.*, 2023; Auteri *et al.*, 2015; Cai *et al.*, 2020).

$$\nabla p(\vec{x},t) = f(\vec{u}(\vec{x},t)) = -\rho \frac{D\vec{u}(\vec{x},t)}{Dt} + \mu \nabla^2 \vec{u}(\vec{x},t) \quad (1)$$

where,

$$\frac{D\vec{u}(\vec{x},t)}{Dt} = \frac{\partial \vec{u}(\vec{x},t)}{\partial t} + (\vec{u}(\vec{x},t)\cdot\nabla)\,\vec{u}(\vec{x},t) \quad (2)$$

A similar but alternative approach is to take the divergence of Equation 1 to form a Poisson equation for pressure as shown in Equation 3, using a continuity equation. Due to the elliptical nature of this equation, well-defined boundary conditions are required at all boundaries. The choice and pattern of Dirichlet and Neumann boundary conditions has been studied extensively (Pan *et al.*, 2016).

$$\nabla^2 p(\vec{x},t) = f(\vec{u}(\vec{x},t)) = -\rho \nabla\cdot(\vec{u}(\vec{x},t)\cdot\nabla)\,\vec{u}(\vec{x},t) \quad (3)$$

The literature to date has emphasized that each of these methods can work given the right conditions (i.e. accurate velocity information for source calculations, appropriate boundary conditions, well-constructed numerical schemes, and sufficient domain extents). However, each method has its own advantages and disadvantages. The averaged path integration technique (Liu & Moreto, 2020) is an iterative method of integrating the source term, derived from measured velocity fields, for pressure (Liu & Katz, 2006). By varying the paths of the integrations through the solution domain, propagation of error due to spurious velocity information is somewhat constrained and boundary conditions are avoided. This process requires a large number of iterations to achieve a converged solution and a physical notion of the pressure somewhere to fix the integration constant. Alternatively, a boundary value problem can be formed which requires some combination of Dirichlet and Neumann boundary conditions. The Poisson solution method is sensitive to amplification of error in the initial velocity fields due to the inherent spatial derivatives, the aspect ratio of the domain, and the selection of boundary conditions (Pan *et al.*, 2016). A hybrid method of boundary condition regularization shown by Pryce *et al.* (2024) can also be used, in which the boundary values for pressure are integrated from the measured velocity fields before being used as Dirichlet boundary conditions to solve the pressure Poisson equation as in Equation 3. This technique provides a reasonable trade-off between accuracy and computation time so as to be practical for laboratory scale investigations.

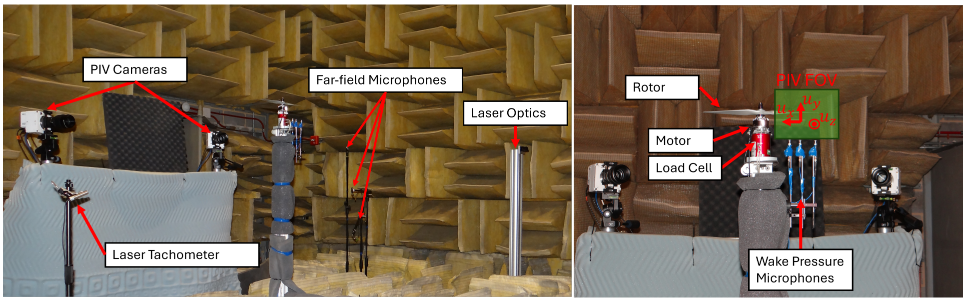

Figure 1. Labeled pictures of the Anechoic test facility with PIV field of view (FOV) and PIV coordinate system.

These methods can be interpreted as deterministic, point wise pressure solution strategies and are often ill-posed and ill-suited for noisy, planar, or otherwise uncertain velocity data common to experiments. Recent approaches have also been formed that align with that fact the pressure reconstructions in these cases should often be looked at probabilistically, with non-uniform uncertainty in different regions of a given flow (Zhang *et al.*, 2019, 2020*a*; Azijli *et al.*, 2016) and that these reconstructions may be treated as statistical inversion problems rather than straightforward PDE inversion (Zhang *et al.*, 2020*b*).

In this work, a weighted variational inverse problem corresponding to the maximum a posteriori (MAP) estimate under spatially varying Gaussian uncertainty models is solved to reconstruct pressure from noisy, partial non-volumetric velocity measurements of the rotor wake. A minimization equation for pressure is formed (Equation 4) with forcing derived from the Navier-Stokes equations (Equation 5), populated with the available velocity terms u and v from the planar PIV measurements. The formulation incorporates adaptive confidence weighting based on force magnitude and local integrability consistency, while preserving adjoint consistency and mask-aware discrete operators. This framework also allows for the analysis of data with measurement noise, uncaptured 3D-effects, discretization error, and non-integrable forcing components.

$$\hat{p} = \arg\min_{p} \Big[\|W_G(Gp-f)\|_2^2 + \|W_D(Dp-g)\|_2^2 + \|W_C(Cp-c)\|_2^2 + \frac{1}{\sigma_p^2}\|p\|_2^2 \Big] \tag{4}$$

$$\nabla p \approx \mathbf{f} = -\rho\left(\frac{\partial \mathbf{u}}{\partial t} + \mathbf{u}\cdot\nabla\mathbf{u}\right) + \mu\nabla^2\mathbf{u} \tag{5}$$

where:

p is the unknown pressure field,
G is the discrete gradient operator,
f is the velocity-derived forcing,
D is a Neumann boundary operator,
g is the appropriate boundary forcing,
c denotes sensor/measurement pressures,
σ_p controls prior regularization.

The first, dominant terms, $\|W_G(Gp-f)\|_2^2$, enforces consistency between reconstructed pressure gradients and the momentum equation forcing and is spatially weighted by encoding spatially varying confidence in the inferred pressure-gradient forcing using both forcing magnitude and local physical consistency diagnostics. In particular, elevated curl and divergence magnitudes are interpreted as indicators of non-conservative forcing, unresolved three-dimensional motion, discretization error, or poor vector reconstruction, leading to local relaxation of the governing pressure-gradient constraints. The governing-constraint uncertainty scale, σ_G, is estimated adaptively from the reconstruction residuals, $r_G = Gp - f$, using a median absolute deviation ($MAD = median(\|x - median(x)\|) \approx 0.67449\sigma$) estimate of the reconstruction residual. The uncertainty is computed as:

$$W_G(\|f\|, \|\nabla\times f\|, \|\nabla\cdot u\|) = \frac{1}{\sigma_{edge}} \tag{6}$$

$$\sigma_{edge} = \frac{\sigma_G}{\sqrt{c_{div}c_{curl}c_f}} \tag{7}$$

$$\sigma_G = 1.4826 \quad median(\|r_G - median(r_G)\|) \tag{8}$$

The MAD estimator provides a robust estimate of residual spread that is significantly less sensitive to outliers than conventional variance-based estimators. This is particularly important in pressure reconstruction problems, where localized discretization errors, unresolved three-dimensional flow effects, and non-conservative forcing can produce heavy-tailed residual distributions. The factor: 1.4826 is the standard scaling that makes the MAD estimator asymptotically equivalent to the standard deviation for Gaussian distributions. The baseline uncertainty scale is further weighted by confidences generated from the governing pressure gradient constraints, where P_{90} denotes $90th$ percentile values of a give value.

$$c_f = \frac{\|f\|}{P_{90}(\|f\|)} \tag{9}$$

$$c_{div} = \frac{1}{1+\|\nabla\cdot f\|/P_{90}(\|\nabla\cdot f\|)} \tag{10}$$

$$c_{curl} = \frac{1}{1+\|\nabla\times f\|/P_{90}(\|\nabla\times f\|)} \tag{11}$$

This reconstruction then takes the form of a weighted least-squares problem in which weak or noisy regions are downweighted, representing low-confidence regions. The second term, $\|W_D(Dp-g)\|_2^2$, represent Neumann boundary conditions in which $\frac{\partial p}{\partial n} = g$ is enforced with $g \approx 0$ on outer boundaries while $g \approx n \cdot f$ on immersed boundaries (rotor in this case). Uncertainty levels are assigned different values at body and out boundaries and also based on the magnitude of the local forcing. The third term, $\|W_C(Cp-c)\|_2^2$, represents pressure measurements taken at the lower boundary of the PIV domain using pressure microphones synchronously obtained with the PIV. These measurements help suppress drift and remove global pressure ambiguity. Uncertainty levels are assigned on a per sensor basis relative to the sensors measured standard deviations, penalizing values outside a given distribution of measured pressure values. The fourth and final term, $\frac{1}{\sigma_p^2}\|p\|_2^2$, is a Gaussian prior that regularizes ill-constrained regions and imposes a penalty on smoothness of the pressure reconstruction.

The weighted least squares system can be represented in the form of $Ap \approx b$ as:

$$A = \begin{bmatrix} W_G G \\ W_D D \\ W_C C \\ \sigma_p^{-1} I \end{bmatrix}, \qquad b = \begin{bmatrix} W_G f \\ W_D g \\ W_C c \\ 0 \end{bmatrix}. \tag{12}$$

with corresponding normal equations:

$$A^T A = G^T W_G^2 G + D^T W_D^2 D + C^T W_C^2 C + \sigma_p^{-2} I. \tag{13}$$

The pressure unknowns are defined at cell centers, in a finite-volume formulation, while pressure gradients are evaluated on cell edges, defined by neighboring values. The forcing terms are projected onto edge-centered values also, preserving directional information and adjoint operators. The edge formulation allows uncertainty weighting to be applied to the individual edge gradient constraints and handle time-varying domain masks (rotor in this case). The system of equations is solved using a matrix-free Krylov formulation rather than assembling large sparse matrices, such that the algorithm only defines Ap and $A^T r$ with residual r. These operators are formed via discrete gradient operators, weighted residual projections, and adjoint edge accumulations (Gunzburger, 2003; Borzi & Schulz, 2012; Greenbaum, 1997; Giles & Pierce, 2000; Ferziger & Perić, 2002). While reconstructions remain inherently ill-conditioned due to noise amplification due to differentiation, this solution strategy improves conditioning by avoiding forming the explicit normal equations $A^T Ab = A^T b$.

The recovered pressure information from this methodology can be viewed as a weak-form pressure reconstruction with associated trust-region information informing where, $\nabla p \approx f$ is physically consistent and statistically reliable. Therefore the inverse problem becomes informative only where the velocity-derived forcing field is sufficiently resolved, dynamically dominant, and approximately compatible with a conservative gradient field. In regions that are more weakly forced or noisy, uncertainty grows and contributions due to the prior are more prominent. The adaptive weighting framework produces a mapping for regions of high confidence and regions of low confidence or lower observability.

In the current application, the method assumes that measured in-plane velocity forcing dominates the local pressure evolution while allowing for the fact that strong three-dimensional velocity regions will introduce inconsistency in the overall forcing condition.

1 RESULTS

The mean vertical velocity $\bar{u_y}$ and TKE are shown in Figures 2(a) and 2(b) respectively. A clear wake slip stream contracts towards the rotor center as expected for a rotor flow field, with most of the turbulent energy being contained along the wake slip stream. These mean statistics are not phase averaged and therefore include components related to the rotation of the blades relative to the stationary plane causing the wake slipstream to appear as one smeared region. The region of high-TKE along the blade is due unresolved PIV regions blocked by the blade, which are masked out for the pressure analysis using individual PIV snapshots. An example of this masking and a phase-averaged mean velocity field is shown in Figure 2(c).

The auto-spectra of the wake microphones, which act as boundary conditions for the pressure solver were calculated using Welch's method with 1 Hz bin widths and 50% overlap. These were converted to dB using a reference pressure of 20 μPa. The spectra of the three wake microphones are shown in 2(d) with frequency normalized by the BPF. The wake pressures have interesting features, where the spectra of the microphones far inside ($0.5R$) and outside ($0.95R$) of the wake slip stream have similar features of a mainly broadband turbulent spectrum with tones at the first few BPF harmonics due to the rotating pressure wave that interacts with the microphones. The microphone near the rotor slip-stream $0.66R$ though has stronger tones due to interactions with the periodically passing tip vortices.

Analysis of the pressure fields from the pressure PIV analysis, an example of which is shown in 3(c), for a single snapshot reveal the predictable structure for the vortices shed from the spinning rotor that pass through the measurement plane, that is, a low pressure core at the center of rotation. It can be seen that the probabilistic pressure reconstruction is enforcing physics and prior in regions where PIV traditionally struggles to maintain accuracy, at the core of the vortices.

Figure 5 shows the relevant uncertainty diagnostics used in the weighting of the reconstruction with force. The top row of figures represent residuals minimized during the reconstruction process, where $Gp - f$ captures how well the reconstructed pressure agrees with the measured forcing, $W_g(Gp - f)$ represent where the physics fit of the solver is poor relative to expected uncertainty, and $Dp - g$ captures how well the reconstruction satisfies prescribed boundary conditions. As expected, for the reconstructed pressure snapshot shown in 3(c), the regions with the highest values are those corresponding to the two in-frame vortices and the trailing wake of that intersects the measurement plane. The bottom row of figures give a physical understanding for the residuals as both $\nabla \cdot u$ and $\nabla \times f$ indicate regions of the flow in which non-conservative behavior is present, i.e. out-of-plane gradients, noise or missing vectors, etc. in the velocity field dominate. While this is expected for the measurements performed in this work, the divergence and curl fields are both used to inform the spatial weighting of the physics uncertainty, relaxing $Gp - f$ constraints in regions where they should not be overly enforced.

Figure 4 shows the comparison of spectra for the measured microphones at the edge of the measurement domain

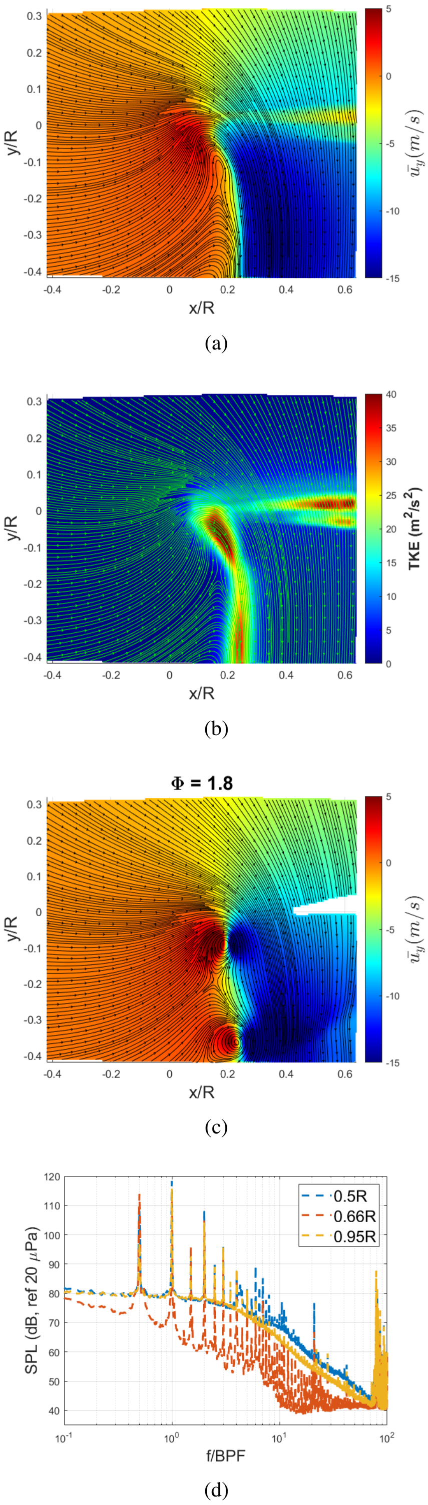

Figure 2. (a) Mean vertical velocity and (b) TKE. (c) Phase averaged velocity field showing masked rotor blade. (d) Autospectrum of the unsteady pressure measured in the rotor wake.

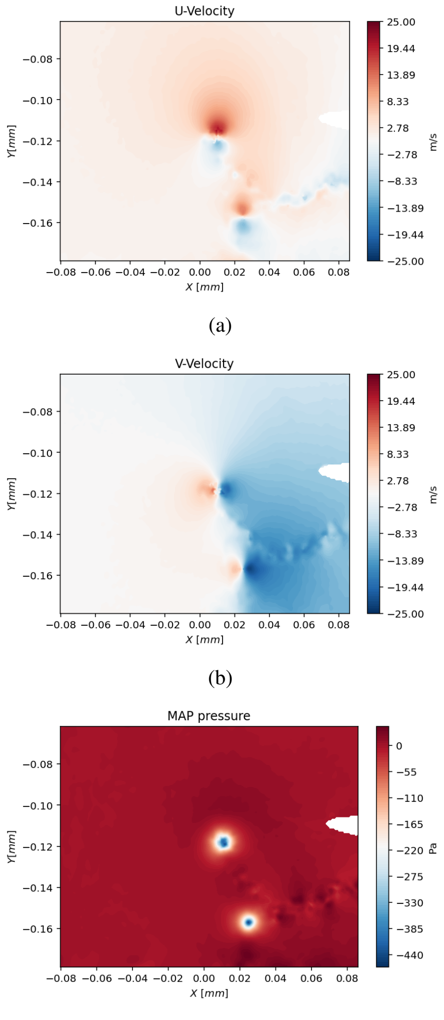

Figure 3. (a) Instantaneous U-velocity, (b) V-velocity, and (c) the corresponding pressure field.

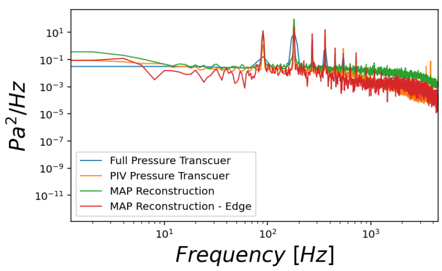

Figure 4. Power spectral density of a pressure microphone at the edge of the PIV domain, for both full- (blue) and PIV-downsampled (orange) rates, and MAP reconstructed pressure estimates at a location near the microphone, for both uniform (green) and nonuniform(red) uncertainty handling of the physics term $(Gp - f)$.

(for both full- and PIV-downsampled rates) and two MAP reconstructed pressure spectra located in regions near-to but not coincident with the microphones. This comparison is informative because the MAP reconstructed pressure does not strictly enforce $\hat{p}_k = p_k$ for any assimilated pressure point. The MAP reconstruction in green and the MAP reconstruction in red are results of two different pressure field reconstructions that differ only in how the uncertainty was handled for the driving physics term, $Gp - f$. In green, the physics term is given a uniform uncertainty that weights the entire domain evenly based on the median of the forcing. The red however uses uncertainty that is weighted by the forcing values at each edge of the gridded domain. It can be seen that both cases capture the tonal character of the pressure, picking up the first few BPF harmonics and the low-frequency broadband turbu-

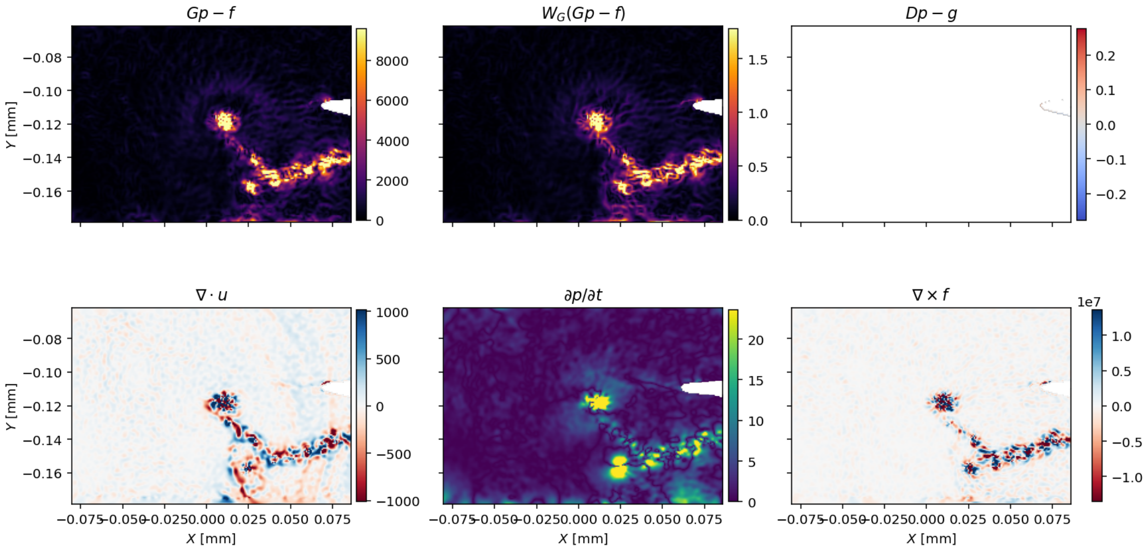

Figure 5. Diagnostic plot used to inform and interpret the uncertainty handling and MAP pressure reconstruction for a given snapshot. The top row of figures represent residual terms minimized during the reconstruction process and the bottom row of figures give a physical understanding for weighting of the residual terms as both $\nabla \cdot u$ and $\nabla \times f$ indicate regions of the flow in which non-conservative behavior is present

lent spectrum. The nonuniform or heteroskedastic weighting for the red data shows that the weighting leads to better resolution of higher frequencies (at $400Hz$ and higher). This is expected as uniform uncertainty weighting does not distinguish between reliable and unreliable forcing regions, causing noisy or non-conservative features to propagate into the pressure reconstruction. At other points in the domain, where microphone measurements are not available for comparison, the difference between scalar weighting and nonuniform weighting holds, with nonuniform weighting showing better spectral roll-off.

2 Future Work

In this study, the unsteady pressure field in the wake of a hovering UAS rotor was reconstructed using high-speed PIV and microphone data to solve a weighted variational inverse problem corresponding to the maximum a posteriori (MAP) estimate under spatially varying Gaussian uncertainty models to reconstruct pressure. The reconstructed pressure fields physically match those expected for a vortex dominated flow and capture spectral features that were measured via microphone data. Most importantly, the reconstruction methodology allows for the implementation of confidence-based weighting, together with physical diagnositcs based on divergence and curl. These mechanisms allow the governing physics model to relax locally, in regions where the underlying assumptions are less valid, particularly in highly three-dimensional flow structures and in regions affected by discretization errors.

Future work will focus on extending the uncertainty framework of the pressure reconstruction methodology toward a fully adaptive probabilistic formulation, including anisotropic uncertainty estimation and Bayesian inference techniques capable of directly estimating posterior pressure uncertainty.

Additionally, now that a framework for analyzing the unsteady pressure in the wake of hovering UAS rotors exists, this information will be explored with respect to optimal sensor placement and noise modeling strategies with respect to UAS systems.

REFERENCES

Advanced Precision Composites 2026 APC 9x6E Propeller. https://www.apcprop.com/product/9x6e/.

Auteri, F., Carini, M., Zagaglia, D., Montagnani, D., Gibertini, G., Merz, C. B. & Zanotti, A. 2015 A novel approach for reconstructing pressure from piv velocity measurements. *Experiments in Fluids* **56** (2).

Azijli, Iliass, Sciacchitano, Andrea, Ragni, Daniele, Palha, Artur & Dwight, Richard P. 2016 A posteriori uncertainty quantification of piv-based pressure data. *Experiments in Fluids* **57** (5).

Borzi, Alfio & Schulz, Volker 2012 *Computational Optimization of Systems Governed by Partial Differential Equations*. SIAM.

Cai, Zemin, Liu, Yun, Chen, Tao & Liu, Tianshu 2020 Variational method for determining pressure from velocity in two dimensions. *Experiments in Fluids* **61** (5).

Cantos, Sinforiano, Zhou, Peng, MA, Zhida & Li, Yuhong 2024 A numerical study on the reduction of rotor blade-airframe interaction noise through airframe permeability. In *30th AIAA/CEAS Aeroacoustics Conference (2024)*. American Institute of Aeronautics and Astronautics.

Charonko, John J, King, Cameron V, Smith, Barton L & Vlachos, Pavlos P 2010 Assessment of pressure field calculations from particle image velocimetry measurements. *Measurement Science and Technology* **21** (10), 105401.

Curle, N. 1955 The influence of solid boundaries upon aerodynamic sound. *Proceedings of the Royal Society of London. Series A. Mathematical and Physical Sciences* **231** (1187), 505 – 514.

Ferziger, Joel H. & Perić, Milovan 2002 *Computational Methods for Fluid Dynamics*. Springer.

Giles, Michael B. & Pierce, Niles A. 2000 An introduction to the adjoint approach to design. *Flow, Turbulence and Combustion* **65**, 393–415.

Goldschmidt, James, Salvoni, Isabella & Ukeiley, Lawrence S.

2026 Free-stream turbulence effects on fixed pitch rotors in edgewise flight. In *32nd AIAA/CEAS Aeroacoustics Conference (2026)*. American Institute of Aeronautics and Astronautics.

Greenbaum, Anne 1997 *Iterative Methods for Solving Linear Systems*. SIAM.

Gunzburger, Max D. 2003 *Perspectives in Flow Control and Optimization*. SIAM.

Jia, Zhongqi & Lee, Seongkyu 2019 Acoustic analysis of a quadrotor evtol design via high-fidelity simulations. In *25th AIAA/CEAS Aeroacoustics Conference*.

Jia, Zhongqi & Lee, Seongkyu 2020 Acoustic analysis of Urban air mobility quadrotor aircraft. In *International Powered Lift Conference 2020, Held at Transformative Vertical Flight 2020*.

Liu, Xiaofeng & Katz, Joseph 2006 Instantaneous pressure and material acceleration measurements using a four-exposure piv system. *Experiments in Fluids* **41** (2), 227–240.

Liu, Xiaofeng & Moreto, Jose Roberto 2020 Error propagation from the piv-based pressure gradient to the integrated pressure by the omnidirectional integration method. *Measurement Science and Technology* **31** (5), 055301.

van Oudheusden, Bas W. 2013*a* Piv-based pressure measurement. *Measurement Science and Technology* **24** (3), 032001.

van Oudheusden, B W 2013*b* Piv-based pressure measurement. *Measurement Science and Technology* **24** (3), 032001.

Pan, Zhao, Whitehead, Jared, Thomson, Scott & Truscott, Tadd 2016 Error propagation dynamics of piv-based pressure field calculations: How well does the pressure poisson solver perform inherently? *Measurement Science and Technology* **27** (8), 084012.

Pryce, Connor, Li, Lanyu, Whitehead, Jared P. & Pan, Zhao 2024 A simple boundary condition regularization strategy for image velocimetry-based pressure field reconstruction. *Experiments in Fluids* **65** (6).

Rizzi, Stephen, Huff, Dennis, Jr, D, Bent, Paul, Henderson, Brenda, Pascioni, Kyle, Sargent, D, Josephson, David, Marsan, Mehmet, He, Hua & Snider, Royce 2020 Urban Air Mobility Noise: Current Practice, Gaps, and Recommendations. *NASA TP - 20205007433* .

Wiedemann, Arthur D., Fuller, Christopher & Pascioni, Kyle A. 2025 Reducing rotor-airframe interaction noise in drones using a curved support rod. *AIAA Journal* **63** (7), 3030–3034.

Zawodny, Nikolas S. & Boyd, D. Douglas 2020 Investigation of rotor–airframe interaction noise associated with small-scale rotary-wing unmanned aircraft systems. *Journal of the American Helicopter Society* **65** (1).

Zawodny, Nikolas S. & Pettingill, Nicole A. 2018 Acoustic wind tunnel measurements of a quadcopter in hover and forward flight conditions. In *INTER-NOISE 2018 - 47th International Congress and Exposition on Noise Control Engineering: Impact of Noise Control Engineering*.

Zhang, Jiacheng, Bhattacharya, Sayantan & Vlachos, Pavlos P. 2019 Uncertainty-based pressure field reconstruction from piv/ptv flow measurements with generalized least-squares.

Zhang, Jiacheng, Bhattacharya, Sayantan & Vlachos, Pavlos P. 2020*a* Using uncertainty to improve pressure field reconstruction from piv/ptv flow measurements. *Experiments in Fluids* **61** (6).

Zhang, Jiacheng, Brindise, Melissa C. *et al.* 2020*b* 4d flow mri pressure estimation using velocity measurement-error based weighted least-squares. *IEEE Transactions on Medical Imaging* **39** (5), 1668–1680.

Zhang, Junrong, Sakib, Nazmus & Pan, Zhao 2023 Modified (n + 1)d laplacian for smooth pressure reconstruction based on time-resolved velocimetry (1): Analysis and numerics.

Zhu, Yifei, Lin, Defu, Mo, Li, Lv, Peijian & Ye, Jianchuan 2021 Numerical Study of the Aerodynamic Interference of Rotors Imposed on Fuselage for a Quadcopter. *IEEE Access* **9**, 150021 – 150036.